Nature Communications

https://doi.org/10.1038/s41467-026-70315-4

Article in Press

Large megathrust earthquakes in cold mantle wedge corners under lawsonite blueschist facies

Received: 17 March 2025

Accepted: 20 February 2026

Cite this article as: Zhang, H., Barbot, S., Yang, Z. *et al.* Large megathrust earthquakes in cold mantle wedge corners under lawsonite blueschist facies. *Nat Commun* (2026). https://doi.org/10.1038/s41467-026-70315-4

Hao Zhang, Sylvain Barbot, Zekang Yang, Mingqi Liu, Lei Zhang & John Platt

Large megathrust earthquakes in cold mantle wedge corners under lawsonite blueschist facies

Hao Zhang[1,*], Sylvain Barbot[1], Zekang Yang[2], Mingqi Liu[1], Lei Zhang[2], and John Platt[1]

[1]Department of Earth Sciences, University of Southern California

3651 Trousdale Pkwy, Los Angeles, CA 90089, USA

[2]Institute of Geology, China Earthquake Administration

Chaoyang, Beitucheng W Rd, Beijing, 100017, China

[*]Present address: Seismological Laboratory, California Institute of Technology

1200 E. California Blvd., Pasadena, CA 91125, USA

Correspondence to: Lei Zhang (zhanglei@ies.ac.cn)

Abstract

Giant megathrust earthquakes typically occur above the upper-plate Moho or the 350°C isotherm in warm subduction zones. However, large earthquakes also occur within the mantle wedge corner at 35-55 km depth at cold subduction zones, such as the Kermadec, Japan Trench, and Chilean margins. Here we investigate the frictional behavior of lawsonite blueschist metagreywacke, potentially found in cold subduction channels, to better understand the control of metamorphic grade on such first-order variations in seismogenic depth. We perform velocity-step experiments on metagreywacke gouge from room temperature to 500°C and effective normal stresses from 50 MPa to 320 MPa, capturing the unstable friction regime and the brittle-to-flow transition. The constitutive behavior of metagreywacke indicates a potential seismogenic behavior at high temperatures below the Moho. Large megathrust earthquakes in the mantle wedge corner may develop in the lawsonite blueschist metasediment channel of cold subduction slabs.

Introduction

The dynamics of megathrust earthquakes is governed by the material properties and hydrothermal conditions along the subduction interface [*Harris et al.*, 2017; *Qiu and Barbot*, 2022]. The down-dip extension of large megathrust earthquakes is thought to be thermally and structurally constrained above the 350°C isotherm and the overlying Mohorovičić discontinuity (Moho) [*Gao and Wang*, 2017], corresponding to a thermally activated stability transition of crustal material and the serpentinization of ultramafic rocks in the mantle wedge corner [*Blanpied et al.*, 1995; *Hyndman et al.*, 1997; *Scholz*, 1998; *Oleskevich et al.*, 1999; *Hyndman and Peacock*, 2003; *Wada and Wang*, 2009; *Hyndman*, 2013; *Goswami and Barbot*, 2018; *Nanjundiah et al.*, 2020; *Bassett et al.*, 2025]. Slow-slip events and tremors are typically found at greater depths in the mantle wedge corner [*Beroza and Ide*, 2011; *Audet and Kim*, 2016; *Bürgmann*, 2018], in regions associated with metamorphism and dehydration of the forearc mantle wedge [*Gao and Wang*, 2014]. The thermal and structural controls on the down-dip extent of the seismogenic zone are supported by the depth distribution of seismic moment release [*Bilek and Lay*, 2018], the negative gravity anomaly running parallel to the continental shelf [*Song and Simons*, 2003], and the internal structure of the forearc [*Miura et al.*, 2005; *Saffer and Tobin*, 2011]. Additional controls on megathrust seismicity include the roughness of the subducted seafloor [*Bassett et al.*, 2025; *Gao and Wang*, 2014], the presence of a subduction channel composed primarily of sedimentary rocks and their metamorphic equivalent [*Julve et al.*, 2024], the distribution and migration of fluids [*Nakajima et al.*, 2001; *Huang et al.*, 2025], and the presence of splay faults and folds in the upper-plate [*Sathiakumar and Barbot*, 2021; *Sathiakumar et al.*, 2024; *Julve et al.*, 2025; *Qiu and Barbot*, 2022].

However, large earthquakes occasionally initiate, propagate, and remain entirely confined within the mantle wedge corner. Recent, well-documented examples include the 2021 M_{W} 8.1 Kermadec earthquake, which ruptured the Kermadec subduction interface from 20 to 50 km depth [*Zeng et al.*, 2025; *Ye et al.*, 2025] and the 2007 M_{W} 7.7 Tocopilla earthquake, which ruptured the Northern Chile plate interface from 30 to 60 km depth, well below the continental Moho [*Peyrat et al.*, 2010; *Wang et al.*, 2025]. The frequent occurrence of M_{j} 7 earthquakes at depths of 40 to 60 km along the Japan Trench suggests a megathrust rupture underneath the mantle wedge corner [*Barbot*, 2020]. Such large earthquakes below the upper-plate Moho are associated with cold subduction zones characterized by rocks of lower metamorphic grade.

The seismogenic potential of subduction megathrusts is generally delineated by structural, hydrothermal, and compositional boundaries (Figure 1a,b). However, the lithological composition of the plate interface is poorly known, as the megathrust may cut the subducting oceanic crust, the overlying accretionary prism, or a mediating sediment channel with various proportions of quartz and phyllosilicates, depending on the protolith [*Julve et al.*, 2024]. Cold and warm subduction zones produce rocks in different metamorphic grades (Figure 1c) [*Frost and Frost*, 2019]. Warm subductions, such as the Nankai [*Peacock*, 2009], Cascadia, and Central American [*Syracuse et al.*, 2010], expose the plate interface to pumpellyite greenschist, greenschist, and epidote blueschist metamorphic conditions. In contrast, cold subduction zones, such as the Japan Trench, Northern Chile [*Julve et al.*, 2025], and Kermadec [*Gao and Wang*,

2014], turn protolithic material to lawsonite-albite-chlorite and lawsonite blueschists conditions with increasing depth, potentially changing the dominant mineral composition of the plate interface and its associated mechanical properties. Although slow-slip events can be found in warm and cold subduction zones, such as the deep episodic tremor and slip at warm Cascadia [*Brudzinski and Allen*, 2007] and the intense slow-slip activity of the cold Costa Rica plate interface [*Dixon et al.*, 2014], deep mantle wedge earthquakes seem to occur exclusively along cold subducted slabs.

The scarcity of large megathrust earthquakes in warm mantle wedge corners is consistent with experimental results on greenschist [*Barbot et al.*, 2025; *Guvercin et al.*, 2025] and epidote blueschist [*Okamoto et al.*, 2020]. The Pelona, Rand Mountain, and Portal greenschists associated with the Farallon subduction [*Chapman*, 2017] all exhibit steady-state velocity strengthening at temperatures above 350°C under effective normal stresses of 100–300 MPa [*Barbot et al.*, 2025; *Guvercin et al.*, 2025]. Similarly, synthetic actinolite–chlorite gouge is velocity strengthening at temperatures above 400°C under effective normal stresses of 50–200 MPa [*Okamoto et al.*, 2020]. These data indicate predominantly velocity-strengthening behavior under warm mantle wedge corner conditions, precluding earthquake nucleation. In contrast, experimental work on lawsonite blueschist indicates velocity-weakening above 300°C at low effective normal stress [*Sawai et al.*, 2016], but the frictional behavior under the pressures and temperatures relevant to cold mantle wedge corners remains unknown.

Here, we examine the frictional behavior of lawsonite-blueschist–facies metagreywacke, a metasediment common in the sediment channel of cold subduction zones, over a broader temperature and pressure range. We conduct triaxial velocity-step tests on synthetic gouge from room temperature to 500°C under effective normal stresses of 50–320 MPa, spanning regimes from unstable friction to the brittle–ductile transition. The mechanical data provide insights into the seismogenic and rupture mechanisms in the mantle wedge corner of cold subduction zones. In the Results section, we describe the mineral composition and metamorphic grade of the metagreywacke sample, and present velocity-step experiments conducted using a triaxial apparatus under varying hydrothermal conditions, pressures, and loading rates. In the Discussion section, we calibrate a constitutive model to capture the different regimes of frictional stability of metagreywacke. We use seismic cycle simulations and steady-state stability models to discuss the relevance of lawsonite blueschist for the 2021 Mw 8.1 Kermadec earthquake and mantle-wedge seismicity at the Japan Trench. We propose that large ruptures within the mantle wedge corner on cold slabs can be promoted by subducted metasediment in lawsonite blueschist facies.

Results

Catalina metagreywacke

To better understand the role of metamorphic grade on megathrust seismicity, we investigate the mechanical properties of a metagreywacke. Greywacke, a type of sedimentary rock incorporating more feldspar and volcanic rock fragments than most sandstones, is commonly associated with the accretionary prism of subduction zones, accumulating as deep marine sediment. Metagreywacke, the metamorphic counter-

part, may play an important role in megathrust dynamics when incorporated in a metasediment channel at the plate interface.

We conduct laboratory deformation experiments on a natural metagreywacke sample (PG178) collected from Santa Catalina Island, California (Figure S1). The Catalina Schist terrane, associated with the Franciscan Complex of the California Coast Ranges, consists of several distinct units that vary in age, metamorphic history, and structural evolution [*Platt et al.*, 2020]. We sample PG178 in the island central region at 118.506°W, 33.426°N in the Catalina Blueschist Unit, where metamorphosed greywacke sandstones and shales account for approximately 80% of the outcrop area, the remainder consisting of metamorphosed conglomerates, chert, basaltic volcanic rocks, and irregular bodies of serpentinite and associated lithologies.

Thin section analysis (Figure 2) indicates that PG178 contains 300-500 µm diameter detrital grains of quartz, feldspar, and lithic fragments in an originally silty clay matrix. The protolith was likely a greywacke sandstone, characteristic of sediments deposited by turbidity currents in subduction zone trenches. Detrital K-feldspar has largely been replaced by fine-grained white mica. Detrital plagioclase contains metamorphic lawsonite prisms, irregular clots and fibrous aggregates of jadeitic pyroxene, and small needles of amphibole within relict albite. Lithic fragments and matrix material now form aggregates of chlorite, white mica, lawsonite, and amphibole with minor titanite and fine-grained organic carbon. The amphibole in the rock is too fine-grained to identify under the optical microscope, but is likely glaucophane, as glaucophane is abundant in metabasaltic rocks close to the sample location. The metamorphic mineral assemblage is consistent with the blueschist facies. The sample has a weak cleavage defined by oriented sheet silicates, lawsonite, and amphibole, forming narrow bands that wrap around the detrital minerals; this cleavage is likely to have formed by pressure solution during the blueschist-facies metamorphic event. The thin section analysis is consistent with the X-ray diffraction (XRD) results (Figure S2), which indicate a composition of 31% quartz, 26% albite, 19% chlorite, and 13% lawsonite, 9% glaucophane, with minor amounts of muscovite (2%). Raman spectroscopy on carbonaceous material (RSCM) estimates a peak metamorphic temperature of 331 ± 21°C under the pressure of 1.06 ± 0.04 GPa [*Platt and Schmidt*, 2024], corresponding to a depth of 37 km. The blueschist facies mineral assemblage suggests that the graywacke protolith was subducted along a cold slab, similar to those in Southern Chile [*Julve et al.*, 2024], Northern Chile [*Julve et al.*, 2025], and Japan Trench [*Gao and Wang*, 2014]. The presence of lawsonite indicates that the sample did not reach eclogite facies nor epidote blueschist facies conditions, implying that it remained at a relatively low temperature (450°C) before exhumation. In warmer subduction zones, e.g., Nankai [*Peacock*, 2009], Mexico, and Northern Cascadia [*Syracuse et al.*, 2010], temperatures exceeding 450°C can cause lawsonite breakdown, forming garnet and omphacite.

The lawsonite blueschist facies of sample PG178 apply to a broad range of pressure-temperature conditions applicable to cold subduction zones from 20-30 km down to about 70 km depth, spanning the conditions found in the forearc accretionary prism and the mantle wedge corner (Figure 1a). This broad depth range provides a valuable opportunity to investigate the frictional behavior along the interface of cold subduction zones in various hydrothermal and pressure conditions for a given protolith.

Laboratory observation

We conduct velocity-step experiments under hydrothermal conditions (Figure S3) using a powder derived from PG178 (Methods). A series of experiments is performed under a constant pore fluid pressure of 30 MPa. To prevent pressure fluctuations during stick-slip motion and oscillatory slip, the confining pressure is maintained constant by the servo-system throughout each individual experiment. However, since the relationship between confining pressure and normal stress is influenced by the gouge friction coefficient, which varies between experiments, the confining pressure is adjusted accordingly for different experiments. This ensures that the effective normal stress is maintained at approximately 50, 100, 200, or 320 MPa for each experiment. To assess the velocity dependence of the effective friction coefficient, we step the loading velocity in a sequence starting at 1.2 µm/s, followed by decreases to 0.24 and 0.048 µm/s, then increases to 0.24 and 1.2 µm/s. The sequence begins after the sample yields, marking the transition from a rapid increase in shear stress with displacement to a more gradual slope (Figure 3). The normal stress continues to increase slightly after yielding. We do not adjust the confining pressure during each individual experiment but record the actual normal stress at each velocity step. Each velocity step covers a similar slip distance of 0.2-0.3 mm. We repeat the full sequence twice with a total displacement of less than 4 mm. We conduct experiments at temperatures ranging from 100°C to 500°C in 100°C intervals, as well as at room temperature (∼25°C), for all four effective normal stresses. In total, we perform 24 experiments, each lasting approximately 8 hours, which includes time for sample preparation, loading, and velocity step execution.

The evolution of the friction coefficient with loading displacement and its response to velocity steps is systematically recorded (Figure 3), revealing dependencies on ambient temperature, effective normal stress, and slip rate. During the velocity step sequence, the sample exhibits continuous hardening with cumulative slip. This effect is removed by detrending the raw data in the following analysis. The second velocity-step sequence, starting from the velocity step from 0.24 µm/s to 1.2 µm/s, exhibits more stable behavior than the first one, likely due to textural maturation under cumulative stress. Therefore, subsequent analyses focus on the second sequence, except for the experiment at 30°C and 320 MPa, where the jacket broke after the first sequence. At each velocity step, the frictional resistance directly responds to the slip rate change, the so-called direct effect, followed by an evolutionary phase toward a new steady-state level. The difference in friction coefficient between the steady states before and after the velocity step corresponds to the steady-state response. At 30°C and 100°C, the frictional behavior is slip-rate- and state-dependent, showcasing steady-state velocity-strengthening across all imposed velocities. At 200°C, velocity-neutral behavior emerges, followed by a transition to velocity-weakening at 300°C, as indicated by the opposite direct and steady-state responses. In this study, we refer to rate-dependent deformation, where evolutionary effects are negligible, as ductile behavior. At 300°C and 320 MPa, ductile behavior is observed during the velocity step from 0.24 µm/s to 0.048 µm/s. At higher temperatures of 400°C and 500°C, the direct response to velocity steps increases significantly, with ductile behavior dominating all velocity steps at 320 MPa. The experiments reveal a clear progression from velocity-strengthening to velocity-neutral, and eventually to velocity-weakening as ambient temperature increases (Figure 4a). Similarly, a transition from brittle to ductile behavior occurs with increasing effective normal stress

(Figure 4b).

Scanning electron microscopy (SEM) of the deformed samples reveals a distinct microstructure for different temperatures and pressures (Figure S4). Comparison of shear structures between samples deformed at 100°C and 400°C under the same effective normal stress highlights the development of S-C fabric and the activation of volume deformation at higher temperatures. While the samples with velocity-weakening behavior at 300°C and low effective normal stress develop localized Riedel shear bands, the velocity-strengthening samples at temperatures over 300°C and 200 MPa effective normal stress develop S-C fabric. These observations suggest the activation of viscous deformation at larger effective normal stress, possibly involving intergranular pressure-solution creep [*de Meer and Spiers*, 1999].

We use the empirical slip-rate- and state-dependent friction framework [*Dieterich*, 1979; *Ruina*, 1983], to estimate the direct effect velocity dependence parameter

$$a = \frac{\partial \mu}{\partial \ln V} \ , \tag{1}$$

and the steady-state velocity dependence parameter

$$a - b = \frac{\partial \mu_{ss}}{\partial \ln V} \ , \tag{2}$$

where μ and μ_{ss} are the friction coefficient and its value at steady state, respectively, and V is the instantaneous slip-rate, as a function of background temperature, effective normal stress, and slip-rate. We estimate the effective frictional properties using the RSFit3000 package [*Skarbek and Savage*, 2019], which provides best-fit parameters using the aging law and the slip law [*Ruina*, 1983]. A frictional response characterized by $a-b<0$ is referred to as steady-state velocity weakening, a necessary condition for spontaneous nucleation under isothermal conditions. The best-fit parameters derived from the two evolution laws exhibit minimal differences for most velocity steps in this study. The fitted values of a and $a-b$ are presented in Figure 5.

Under a low effective normal stress of 50 MPa, the mechanical response of metagreywacke gouge exhibits two distinct constitutive regimes. At low temperatures, steady-state velocity-strengthening dominates, while velocity-weakening appears at higher temperatures, with the transition temperature increasing as the slip rate rises. At higher effective normal stresses of 200 MPa and above, the amplitude of $a-b$ in the velocity-weakening regime diminishes, and a ductile regime characterized by higher a and near-zero b emerges at high temperatures and low slip rates. At 320 MPa, the ductile regime expands, shrinking the velocity-weakening regime, resulting in velocity-strengthening behavior across all temperatures and slip rates. The low-temperature boundary of the velocity-weakening domain remains relatively constant as normal stress increases, but the transition from velocity weakening to the ductile regime shifts significantly. This indicates that the brittle to ductile transition in metagreywacke is strongly influenced by effective normal stress.

Discussion

Constitutive model

To capture the three distinct regimes observed in laboratory data, including the transition between brittle and ductile behavior, we adopt a constitutive model with thermal activation and a pressure-dependent activation temperature [*Barbot et al.*, 2025; *Barbot*, 2025]. The model incorporates one brittle, one semi-brittle, and one ductile deformation mechanism, alongside an evolution law featuring two healing mechanisms regulating the size of micro-asperities on faults (Methods). Here, the semi-brittle mechanism refers to slip-rate- and state-dependent deformation with a low stress power exponent, while the ductile mechanism refers to rate-dependent, non-elastic deformation with a power exponent possibly much larger than unity.

The constitutive model replicates the values of a and $a-b$ across varying slip rates, temperatures, and effective normal stresses with the constant constitutive parameters shown in Table 1. We optimize the preferred model parameters by pair-wise parameters grid search (Figure S5). The constitutive model requires more parameters than for experiments on other rocks [e.g., *Barbot and Zhang*, 2023; *Barbot et al.*, 2025] to account for the brittle-to-semi-brittle and brittle-ductile transitions. The common parameters remain consistent in magnitude across different rocks, demonstrating the effectiveness of the constitutive framework across lithology.

The model successfully captures the transition from steady-state velocity-strengthening friction to velocity-weakening friction at low temperature, as well as the stability transition to ductile deformation at high temperatures and high effective normal stress (Figures 6 & 7). Additionally, the model accurately reproduces the frictional response to velocity steps in both the brittle and ductile regimes using a spring-slider model with finite stiffness (Figure 4c). We apply a uniform machine stiffness of 100 GPa/m across the three simulations in Figure 4c to approximate the deformation of the experimental apparatus, although machine stiffness may vary in other velocity step tests. The constitutive model effectively predicts the overall transition in frictional behavior and the detailed response to velocity steps, capturing the complex frictional properties of metagreywacke in various hydrothermal and pressure conditions. The model can be used to probe the frictional behavior of the subduction megathrust during various phases of the seismic cycle.

Earthquake nucleation within cold mantle wedge corners

Rocks of various mineral compositions may accumulate near the frontal thrust across geologic time scales to eventually be entrained in the subduction channel. As a result, different protoliths may be found in lawsonite blueschist facies, except for the common presence of key minerals representative of this metamorphic grade, such as lawsonite or glaucophane. The composition of the protoliths, particularly with various quartz and feldspar content, may affect the frictional properties of the interface [*Niemeijer et al.*, 2008; *Di Toro et al.*, 2004]. As the mineral composition is stable under a given metamorphic grade [*Frost and Frost*, 2019], our sample lithology may be found under any pressure-temperature conditions in lawsonite blueschist facies, covering the wide pressure-temperature regime of cold subducted slabs. Ac-

cordingly, we discuss the relevance of lawsonite blueschist metagreywacke for megathrust dynamics in cold subduction zones.

We first model the frictional properties along the interface of the Kermadec subduction zone, an intra-oceanic, volcanically active, convergent plate boundary [*de Ronde et al.*, 2001], assuming greywacke deposition and subduction in the accretionary prism. The oceanic arc Moho in the Kermadec subduction zone is located at approximately 17 km [*Bassett et al.*, 2016]. In 2021, a M_{W} 8.1 megathrust earthquake occurred at a centroid depth of 55 km, preceded by a M_W 7.4 foreshock at a depth of 45 km, corresponding to the mantle wedge corner [*Ye et al.*, 2025]. The thermal structure of the Kermadec subduction zone [*Gao and Wang*, 2014] features an increase of the interface temperature from 150°C at 15 km depth to 600°C at 75 km depth (Figure 8a). A steady-state effective normal stress model for the Kermadec subduction zone with an over-pressurized subducting sedimentary channel [*Kaneki and Noda*, 2023] indicates a peak effective normal stress of 85 MPa at 35 km depth, which we extend to greater depths (Figure 8a).

The instantaneous fault slip-rate evolves within about 12 orders of magnitude during the interseismic, coseismic, and postseismic phases of the seismic cycle. As frictional properties are functions of instantaneous slip-rate, temperature, and effective normal stress, we determine frictional stability at various depths under slip-rates representative of different stages of typical earthquake nucleation. We consider a locked interface with a fault slip rate of 10^{-8} mm/s, a creeping interface sliding at the plate convergence rate of 10^{-6} mm/s, and earthquake nucleation with slip rates approaching 10^{-4} mm/s (Figure 8b,c). For each depth, we simulate the steady-state frictional properties as described in the previous section for the spring-slider simulations, taking the various assumed fault slip rates as post velocity V_2. As the frictional resistance at these low slip-rates generates negligible heat, we assume a steady-state interface temperature. We do not consider thermal and hydraulic transport along the interface.

For all slip-rates considered, metagreywacke exhibits brittle frictional behavior within the lawsonite blueschist facies depth range. At slip-rates associated with creep or earthquake nucleation, the modeled velocity dependence of friction at steady state shows a transition from velocity strengthening at shallower depths to velocity weakening at greater depths. While the depth of this transition increases with slip-rate, most of the lawsonite blueschist grade still exhibits velocity weakening at slip-rates representative of earthquake nucleation. Most of the slip in the 2021 Kermadec earthquake is confined within the velocity-weakening regime at earthquake nucleation loading rates (Figure 8b), suggesting that the presence of metagreywacke on the subduction interface may promote the nucleation and propagation of this megathrust event.

Next, we consider the frictional regime of metagreywacke in the physical conditions of the Japan Trench, where the oceanic Pacific Plate subducts beneath the continental Okhotsk Plate, forming a large accretionary prism. While the 2011 Mw 9.1 Tohoku-Oki earthquake initiated in the shallow section of the plate interface to eventually propagate into the mantle wedge corner, smaller earthquakes with local magnitudes greater than 7 occur below the arc Moho. The thermal structure of the Japan Trench is similar to Kermadec [*Gao and Wang*, 2014], with an increase of interface temperature from 150°C at 15 km to 600°C at 75 km (Figure 8a). We use the same effective hydraulic model as for Kermadec, and the frictional stability is modeled at the same three slip-rates. The transition depth between velocity-weakening

and velocity-strengthening friction is slightly greater in the Japan Trench than in the Kermadec, as the interface temperature is slightly lower in the Japan Trench. We compare the slip distribution of the 1978 M_W 7.7 Miyagi-Oki earthquake [*Yamanaka and Kikuchi*, 2004], the 2021 M_W 7.1 Namie earthquake, the 2021 M_W 7.0 Ishinomaki earthquake, and the 2022 M_W 7.3 Namie earthquake [*Goldberg et al.*, 2022]. The rupture of these events is confined within the velocity-weakening regime at earthquake nucleation slip rates, further supporting the idea that metagreywacke may play a key role in megathrust dynamics within the mantle wedge corner on cold slabs. Although the temperature and effective normal stress conditions in Figure 8 do not reach the fully ductile regime — so the transition from velocity-weakening back to velocity-strengthening is not captured — the trend from approximately 40 km to 70 km depth suggests a progressive shift toward velocity-neutral friction. The observed variation in $a - b$ with depth likely reflects a gradual change in dominant deformation mechanism. At shallower depths, frictional behavior is governed by dilatant, brittle processes such as micro-fracturing [*Scholz*, 1968] and gouge comminution [*Morrow and Byerlee*, 1989], leading to velocity-weakening behavior. With increasing depth and temperature, pressure-solution creep [*Fagereng and Den Hartog*, 2017] may become more active, promoting compactive, stable sliding and resulting in more ductile behavior.

We further illustrate the potential role of metagreywacke in mantle-wedge corner seismicity using two-dimensional numerical simulations of the seismic cycle at the Japan Trench (Figure 9). The model extends from 40 to 60 km depth with a dip angle of 15° with a constant effective normal stress of 125 MPa and a temperature increasing from 300°C at 3°C/km. We sample the megathrust interface using 800 samples of 100 m length, sufficiently small to resolve the cohesion zone at the rupture front. We impose a long-term slip-rate of 10 cm/yr. The frictional properties are governed by the constitutive framework and the evolution of fault slip follows the law of conservation of momentum. Although different rocks may be present at the Japan trench mantle wedge corner, we test a lithologic model dominated by metagreywacke with the constitutive parameters of Table 1. The model uses the boundary integral method with the radiation-damping approximation implemented in the software "Unicycle" [*Barbot*, 2018, 2019b], which is validated against other numerical methods [*Erickson et al.*, 2020; *Jiang et al.*, 2022]. The model captures all phases of the seismic cycle, including the spontaneous nucleation and propagation of earthquakes and the interseismic period. However, the quasi-dynamic approximation leads to unrealistic rupture durations. Furthermore, the model ignores the additional weakening from thermal pressurization [*Ferri et al.*, 2010] or melting [*Brown and Fialko*, 2012] that may occur at seismic slip velocities. The numerical simulations produce sequences of partial and full pulse-like ruptures recurring approximately every 10 to 30 years. With coseismic slip of 2 m, the simulated ruptures reproduce deep seismic events along the Japan Trench.

Laboratory observations and constitutive model indicate brittle, velocity-weakening behavior of lawsonite blueschist metagreywacke over a wide depth range within the mantle wedge corner, facilitating the nucleation and propagation of large sub-Moho earthquakes in cold subduction zones, potentially explaining anomalously deep earthquakes at the Kermadec, Japan Trench, and Chilean margins. The numerical simulations of seismic cycles along the mantle wedge section of a subduction megathrust validate the ability of the constitutive model to extrapolate laboratory data to natural conditions, confirming the

seismogenic potential of metagreywacke under mantle wedge corner conditions.

Methods

Experimental setup and materials

The experiments are performed in a triaxial apparatus with argon gas as the confining medium [*He et al.*, 2007]. This system supports a maximum confining pressure of 300 MPa and operates within a temperature range from room temperature to 600°C. A drilled hole in the specimen allows direct access to the gouge layer for pore fluid pressure up to 200 MPa (Figure S3). Pore pressure is regulated via a feedback-controlled, stepping-motor-driven pressure generator, maintaining an accuracy of ±0.3 MPa. Following the procedure outlined by *He et al.* [2007], we prepare the sample by crushing the metagreywacke and sieving it through a 200-mesh to obtain gouge powder with grain sizes below 74 µm. A 1-mm-thick layer of this gouge is then sandwiched between gabbro forcing blocks, each measuring 20 mm in diameter and 40 mm in total length, with a saw-cut oriented at a 35° angle to the loading axis. The saw-cut surfaces are roughened with 200# abrasive.

Constitutive model

We consider a physical model of sliding friction constrained by experimental observations under various pressure, temperature, and kinematic conditions. Rock friction is modulated by the area of contact junctions [*Dieterich and Kilgore*, 1994, 1996; *Maegawa et al.*, 2015; *Wu and Barbot*, 2025]. We assume that the frictional resistance is proportional to the real area of contact, which depends on the size of micro-asperities and the effective normal stress following [*Barbot*, 2019a, 2024a]

$$\mathcal{A} = \frac{\bar{\sigma}}{\chi_n}\left(\frac{d}{d_0}\right)^{\alpha}\left(\frac{\bar{\sigma}}{\sigma_0}\right)^{-\beta}, \tag{3}$$

where $\mathcal{A} = A_r/A_0$ is the ratio of the real and the nominal area of contact, $\bar{\sigma}$ and σ_0 are the effective normal stress and a reference value, respectively, and d and $d_0 = 1\,\mu\text{m}$ represent the average size of micro-asperities and a reference value, respectively. The proportionality factor χ_n relates to the indentation hardness [*Dieterich and Kilgore*, 1994]. The parameters α and β are power-law exponents, both less than unity. The proportional relationship between the real contact area and frictional resistance is expressed as

$$\tau_y = \mathcal{A}\chi\,, \tag{4}$$

where χ is a material property analogous to plowing hardness. The frictional resistance under non-isothermal and non-isobaric conditions is expressed as [*Barbot*, 2023]

$$\begin{aligned}\frac{V}{V_0} = &\sum_{k=1}^{2}\left(\frac{\tau}{\tau_y}\right)^{n_k}\exp\left[-\frac{Q_k}{R}\left(\frac{1}{T}-\frac{1}{\bar{T}_k}\right)\right]\\ &+\left(\frac{\tau}{\tau_0}\right)^{n_3}\exp\left[-\frac{Q_3}{R}\left(\frac{1}{T}-\frac{1}{\bar{T}_3}\right)\right],\end{aligned} \tag{5}$$

where the subscript $k = 1, 2, 3$ represents the brittle, semi-brittle, and ductile deformation mechanisms, respectively, and n_k, Q_k, and $\bar{T}_k$ are the stress power exponent, the activation energy, and the activation temperature for each deformation mechanism. The stress power exponent n_2 for the semi-brittle mechanism is typically lower than n_1 for the brittle mechanism. The ductile mechanism has a higher stress power exponent n_3 than for high-temperature, high-pressure viscous mechanisms, a tendency also observed in halite [*Noda and Shimamoto*, 2012], granitoids [*Pec et al.*, 2016], and schists [*Okazaki and Hirth*, 2020]. The constant τ_0 is the reference shear strength for the ductile deformation mechanism, assumed independent of confining pressure. Brittle, semi-brittle, and ductile deformation will dominate in specific ranges of temperature and slip-rate controlled primarily by the temperature and energy of activation. To capture the additional sensitivity of the deformation map to pressure, we specify an effective normal stress dependence of the activation temperature, as follows

$$\frac{1}{\bar{T}_k} = \frac{1}{T_k^0} - \frac{\zeta_k R}{Q_k} \ln \frac{\bar{\sigma}}{\sigma_0} \,, \tag{6}$$

where ζ_k is the compressibility factor associated with dilatant deformation for ζ_k positive [*Barbot et al.*, 2025]. Combining Equations (3), (4), (5), and (6), we obtain the slip-rate-, temperature-, and normal-stress-dependent constitutive law

$$\begin{aligned} \frac{V}{V_0} = \sum_{k=1}^{2} \left(\frac{\tau}{\mu_0 \bar{\sigma}}\right)^{n_k} \left(\frac{d}{d_0}\right)^{-\alpha n_k} \left(\frac{\bar{\sigma}}{\sigma_0}\right)^{\beta n_k - \zeta_k} \exp\left[-\frac{Q_k}{R}\left(\frac{1}{T} - \frac{1}{T_k^0}\right)\right] \\ + \left(\frac{\tau}{\tau_0}\right)^{n_3} \left(\frac{\bar{\sigma}}{\sigma_0}\right)^{-\zeta_3} \exp\left[-\frac{Q_3}{R}\left(\frac{1}{T} - \frac{1}{T_3^0}\right)\right] \,, \end{aligned} \tag{7}$$

where each term of the product describes the control of the respective dynamic variable relative to an appropriate representative value for a given deformation mechanism k. The reference values d_0, σ_0, and τ_0 are introduced to make the arguments of the power laws dimensionless and clarify the relevant physical units of the associated dynamic variables, but they do not affect the constitutive behavior.

The size of micro-asperities evolves through plastic deformation at contact junctions and the random rejuvenation of contacts during fault slip [*Barbot*, 2019a]. Normal stress facilitates thermally activated creep at these junctions, contributing to gouge compaction [*Barbot*, 2024a]. The overall process is governed by an evolution law capturing the interplay between contact rejuvenation and plastic deformation of micro-asperities in response to stress and temperature variations, which can be expressed as the aging-law end-member [*Barbot*, 2024b],

$$\frac{\dot{d}}{d} = \sum_{k=1}^{N} f_0 \left(\frac{d}{d_0}\right)^{-p_k} \left(\frac{\bar{\sigma}}{\sigma_0}\right)^{q_k} \exp\left[-\frac{H_k}{R}\left(\frac{1}{T} - \frac{1}{T_k}\right)\right] - \frac{\lambda V}{2h} \,, \tag{8}$$

involving $N = 2$ healing mechanisms. The model incorporates the reference strain-rate $f_0 = 1/\mathrm{s}$, activation energy H_k, activation temperature T_k, asperity-size power exponent p_k, and normal stress power exponent q_k. The gouge layer thickness h and the characteristic strain $1/\lambda$ control the rate of contact rejuvenation. The evolution process can also be described using the slip-law end-member [*Barbot*, 2024b]

$$\frac{\dot{d}}{d} = \frac{\lambda V}{2h} \ln \left\{ \frac{2h}{\lambda V} \sum_{k=1}^{N} f_0 \left(\frac{d}{d_0}\right)^{-p_k} \left(\frac{\bar{\sigma}}{\sigma_0}\right)^{q_k} \exp\left[-\frac{H_k}{R}\left(\frac{1}{T} - \frac{1}{T_k}\right)\right] \right\} \,. \tag{9}$$

The possible pressure dependence of the activation energy of healing is effectively captured in the power exponent q_k, so we do not explicitly incorporate a compressibility factor in Equations (8) and (9). Together, Equations (7) and (8), or Equations (7) and (9), comprehensively describe the frictional behavior of rocks under a wide range of physical conditions. The constitutive framework accounts for the direct and transient responses to velocity steps [*Barbot*, 2019a], temperature steps [*Barbot*, 2024b], and normal stress changes [*Barbot*, 2024a], capturing the stability and brittle-to-flow transitions at different slip rates, temperatures, and effective normal stress [*Barbot and Zhang*, 2023; *Barbot*, 2022, 2023, 2024b; *Barbot et al.*, 2025; *Barbot*, 2025]. This model does not account for melting or strong weakening associated with shear heating. Another potential limitation is the assumed drained conditions at constant pore-fluid pressure, thereby neglecting dilatancy effects.

We simulate the frictional response of metagreywacke to velocity steps numerically for a spring-slider model with infinite stiffness based on Equations (7) and (9), i.e., assuming the slip-law end-member for the evolution law. During a velocity step, the loading velocity increases instantaneously from V_1 to V_2. Under the assumptions of infinite stiffness, the loading rate equals the slip rate at all times. Firstly, we calculate the steady-state shear stress τ and micro-asperity size d under initial velocity by solving equations (7) and (9) with $\dot{d} = 0$ and $V = V_1$. During the velocity step, the shear stress τ exhibits a direct response to the new velocity V_2, while the micro-asperity size d remains unchanged. Contact rejuvenation at a different velocity leads to an evolutionary phase, until a new steady-state micro-asperity size is reached. We solve the evolutionary response using a combination of 4th and 5th order Runge-Kutta method, providing adaptive time steps [*Dormand and Prince*, 1980]. We determine the direct effect parameter a from the change in shear stress normalized by effective normal stress. Similarly, we obtain the steady-state parameter $a - b$ from the difference in steady-state shear stress at velocity V_1 and V_2, normalized by the effective normal stress and the velocity changxe, $\bar{\sigma} \ln(V_2/V_1)$.

Data Availability

The laboratory data used in this study area available in a zenodo.org repository [*Zhang et al.*, 2026].

Code Availability

A demonstration code for simulating velocity-step experiments using the constitutive law proposed in this study is available at https://doi.org/10.5281/zenodo.18529749 [*Zhang et al.*, 2026]. The 'Unicycle' software package, along with the input files for the seismic cycle simulation, can be accessed at: https://bitbucket.org/sbarbot/unicycle.

References

Audet, P., and Y. Kim, Teleseismic constraints on the geological environment of deep episodic slow earthquakes in subduction zone forearcs: A review, *Tectonophysics*, *670*, 1–15, doi:10.1016/j.tecto.2016.01.005, 2016.

Barbot, S., Asthenosphere flow modulated by megathrust earthquake cycles, *Geophys. Res. Lett.*, *45*, 6018–6031, doi:10.1029/2018GL078197, 2018.

Barbot, S., Modulation of fault strength during the seismic cycle by grain-size evolution around contact junctions, *Tectonophysics*, *765*, 129–145, doi:10.1016/j.tecto.2019.05.004, 2019a.

Barbot, S., Slow-slip, slow earthquakes, period-two cycles, full and partial ruptures, and deterministic chaos in a single asperity fault, *Tectonophysics*, *768*, 228,171, doi:10.1016/j.tecto.2019.228171, 2019b.

Barbot, S., Frictional and structural controls of seismic super-cycles at the Japan trench, *Earth, Planets, Space*, *72*(63), doi:10.1186/s40623-020-01185-3, 2020.

Barbot, S., A rate-, state-, and temperature-dependent friction law with competing healing mechanisms, *J. Geophys. Res.*, *127*, e2022JB025,106, doi:10.1029/2022JB025106, 2022.

Barbot, S., Constitutive behavior of rocks during the seismic cycle, *AGU Advances*, *4*(5), doi:10.1029/2023AV000972, 2023.

Barbot, S., Transient and steady-state friction in non-isobaric conditions, *Geochemistry, Geophysics, Geosystems*, *25*(2), e2023GC011,279, doi:10.1029/2023GC011279, 2024a.

Barbot, S., Does the direct effect of friction increase continuously with absolute temperature?, *Proc. Nat. Acad. Sci.*, doi:10.1073/pnas.2405111121, 2024b.

Barbot, S., The slip-rate, state-, temperature-, and normal-stress-dependence of fault friction, *Earthquake Science*, *32*, 1–35, doi:10.1016/j.eqs.2025.03.005, 2025.

Barbot, S., and L. Zhang, Constitutive behavior of olivine gouge across the brittle-ductile transition, *Geophys. Res. Lett.*, *50*(24), doi:10.1029/2023GL105916, 2023.

Barbot, S., S. Guvercin, L. Zhang, H. Zhang, and Z. Yang, Thermobaric activation of fault friction, *Geophys. Res. Lett.*, *52*(6), e2024GL112,959, doi:10.1029/2024GL112959, 2025.

Bassett, D., H. Kopp, R. Sutherland, S. Henrys, A. B. Watts, C. Timm, M. Scherwath, I. Grevemeyer, and C. E. de Ronde, Crustal structure of the kermadec arc from mango seismic refraction profiles, *J. Geophys. Res.*, *121*(10), 7514–7546, doi:10.1002/2016JB013194, 2016.

Bassett, D., D. J. Shillington, L. M. Wallace, and J. L. Elliott, Variation in slip behaviour along megathrusts controlled by multiple physical properties, *Nature Geoscience*, pp. 1–12, doi:10.1038/s41561-024-01617-9, 2025.

Beroza, G. C., and S. Ide, Slow Earthquakes and Nonvolcanic Tremor, *Annu. Rev. Earth Planet. Sci.*, *39*, 271–96, doi:10.1146/annurev-earth-040809-152531, 2011.

Bilek, S. L., and T. Lay, Subduction zone megathrust earthquakes, *Geosphere*, *14*(4), 1468–1500, doi:10.1130/GES01608.1, 2018.

Blanpied, M. L., D. A. Lockner, and J. D. Byerlee, Frictional slip of granite at hydrothermal conditions, *J. Geophys. Res.*, *100*(B7), 13,045–13,064, doi:10.1029/95jb00862, 1995.

Brown, K. M., and Y. Fialko, 'Melt welt' mechanism of extreme weakening of gabbro at seismic slip rates, *Nature*, *488*(7413), 638, doi:10.1038/nature11370, 2012.

Brudzinski, M. R., and R. M. Allen, Segmentation in episodic tremor and slip all along cascadia, *Geology*, *35*(10), 907–910, doi:10.1130/G23740A.1, 2007.

Bürgmann, R., The geophysics, geology and mechanics of slow fault slip, *Earth Planet. Sci. Lett.*, *495*, 112–134, doi:10.1016/j.epsl.2018.04.062, 2018.

Chapman, A. D., The Pelona–Orocopia–Rand and related schists of southern California: A review of the best-known archive of shallow subduction on the planet, *International Geology Review*, *59*(5-6), 664–701, doi:10.1080/00206814.2016.1230836, 2017.

de Meer, S., and C. J. Spiers, On mechanisms and kinetics of creep by intergranular pressure solution, in *Growth, dissolution and pattern formation in geosystems*, pp. 345–366, Springer, 1999.

de Ronde, C. E., E. T. Baker, G. J. Massoth, J. E. Lupton, I. C. Wright, R. A. Feely, and R. R. Greene, Intra-oceanic subduction-related hydrothermal venting, kermadec volcanic arc, new zealand, *Earth and Planetary Science Letters*, *193*(3-4), 359–369, doi:10.1016/S0012-821X(01)00534-9, 2001.

Di Toro, G., D. L. Goldsby, and T. E. Tullis, Friction falls towards zero in quartz rock as slip velocity approaches seismic rates, *Nature*, *427*(6973), 436–439, doi:10.1038/nature02249, 2004.

Dieterich, J. H., Modeling of rock friction 1. experimental results and constitutive equations, *J. Geophys. Res.*, *84*(B5), 2161–2168, doi:10.1029/JB084iB05p02161, 1979.

Dieterich, J. H., and B. D. Kilgore, Direct observation of frictional contacts: New insights for sliding memory effects, *Pure Appl. Geophys.*, *143*, 283–302, doi:10.1007/BF00874332, 1994.

Dieterich, J. H., and B. D. Kilgore, Imaging surface contacts: power law contact distributions and contact stresses in quartz, calcite, glass and acrylic plastic, *Tectonophysics*, *256*(1-4), 219–239, doi:10.1016/0040-1951(95)00165-4, 1996.

Dixon, T. H., Y. Jiang, R. Malservisi, R. McCaffrey, N. Voss, M. Protti, and V. Gonzalez, Earthquake and tsunami forecasts: Relation of slow slip events to subsequent earthquake rupture, *Proc. Nat. Acad. Sci.*, *111*(48), 17,039–17,044, doi:10.1073/pnas.1412299111, 2014.

Dormand, J. R., and P. J. Prince, A family of embedded runge-kutta formulae, *Journal of computational and applied mathematics*, *6*(1), 19–26, doi:10.1016/0771-050X(80)90013-3, 1980.

Erickson, B., et al., The Community Code Verification Exercise for Simulating Sequences of Earthquakes and Aseismic Slip (SEAS), *Seism. Res. Lett.*, doi:10.1785/0220190248, 2020.

Fagereng, Å., and S. A. Den Hartog, Subduction megathrust creep governed by pressure solution and frictional–viscous flow, *Nature Geoscience*, *10*(1), 51–57, doi:10.1038/ngeo2857, 2017.

Ferri, F., G. D. Toro, T. Hirose, and T. Shimamoto, Evidence of thermal pressurization in high-velocity friction experiments on smectite-rich gouges, *Terra Nova*, *22*(5), 347–353, doi:10.1111/j.1365-3121.2010.00955.x, 2010.

Frost, B. R., and C. D. Frost, *Essentials of igneous and metamorphic petrology*, Cambridge University Press, 2019.

Gao, X., and K. Wang, Strength of stick-slip and creeping subduction megathrusts from heat flow observations, *Science*, *345*(6200), 1038–1041, doi:10.1126/science.1255487, 2014.

Gao, X., and K. Wang, Rheological separation of the megathrust seismogenic zone and episodic tremor and slip, *Nature*, *543*(7645), 416–419, doi:10.1038/nature21389, 2017.

Goldberg, D. E., P. Koch, D. Melgar, S. Riquelme, and W. L. Yeck, Beyond the teleseism: Introducing regional seismic and geodetic data into routine usgs finite-fault modeling, *Seism. Res. Lett.*, *93*(6), 3308–3323, doi:10.1785/0220220047, 2022.

Goswami, A., and S. Barbot, Slow-slip events in semi-brittle serpentinite fault zones, *Scientific reports*, *8*(1), 6181, doi:10.1038/s41598-018-24637-z, 2018.

Guvercin, S., S. Barbot, L. Zhang, Z. Yang, J. Platt, C. Seyler, and N. Phillips, Frictional stability of pelona–orocopia–rand schists under hydrothermal conditions and implications for seismic hazards in southern california, *Earth Planet. Sci. Lett.*, *669*, 119,573, doi:10.1016/j.epsl.2025.119573, 2025.

Harris, R. N., G. A. Spinelli, and A. T. Fisher, Hydrothermal circulation and the thermal structure of shallow subduction zones, *Geosphere*, *13*(5), 1425–1444, doi:10.1130/GES01498.1, 2017.

He, C., Z. Wang, and W. Yao, Frictional sliding of gabbro gouge under hydrothermal conditions, *Tectonophysics*, *445*(3-4), 353–362, doi:10.1016/j.tecto.2007.09.008, 2007.

Huang, Y., S. Ide, A. Kato, K. Yoshida, C. Jiang, and P. Zhai, Fault material heterogeneity controls deep interplate earthquakes, *Science Advances*, *11*(9), eadr9353, doi:10.1126/sciadv.adr9353, 2025.

Hyndman, R. D., Downdip landward limit of cascadia great earthquake rupture, *Journal of Geophysical Research: Solid Earth*, *118*(10), 5530–5549, doi:10.1002/jgrb.50390, 2013.

Hyndman, R. D., and S. M. Peacock, Serpentinization of the forearc mantle, *Earth and Planetary Science Letters*, *212*(3-4), 417–432, doi:10.1016/S0012-821X(03)00263-2, 2003.

Hyndman, R. D., M. Yamano, and D. A. Oleskevich, The seismogenic zone of subduction thrust faults, *Island Arc*, *6*(3), 244–260, 1997.

Jiang, J., et al., Community-driven code comparisons for three-dimensional dynamic modeling of sequences of earthquakes and aseismic slip, *J. Geophys. Res.*, *127*(3), e2021JB023,519, doi:10.1029/2021JB023519, 2022.

Julve, J., S. Barbot, M. Moreno, A. Tassara, R. Araya, N. Catalán, J. G. F. Crempien, and V. Becerra-Carreño, Recurrence time and size of Chilean earthquakes influenced by geological structure, *Nature Geoscience*, *17*(1), 79–87, doi:10.1038/s41561-023-01327-8, 2024.

Julve, J., M. Moreno, S. Barbot, and A. Tassara, Impact of upper-plate faulting on megathrust foreshocks: Insights from the 2014 iquique earthquake, *Geophys. Res. Lett.*, *52*(3), e2024GL111,064, doi:10.1029/2024GL111064, 2025.

Kaneki, S., and H. Noda, Steady-state effective normal stress in subduction zones based on hydraulic models and implications for shallow slow earthquakes, *J. Geophys. Res.*, *128*(2), e2022JB025,995, doi:10.1029/2022JB025995, 2023.

Maegawa, S., F. Itoigawa, and T. Nakamura, Effect of normal load on friction coefficient for sliding contact between rough rubber surface and rigid smooth plane, *Tribology international*, *92*, 335–343, 2015.

Miura, S., N. Takahashi, A. Nakanishi, T. Tsuru, S. Kodaira, and Y. Kaneda, Structural characteristics off Miyagi forearc region, the Japan Trench seismogenic zone, deduced from a wide-angle reflection and refraction study, *Tectonophysics*, *407*(3-4), 165–188, doi:10.1016/j.tecto.2005.08.001, 2005.

Morrow, C. A., and J. D. Byerlee, Experimental studies of compaction and dilatancy during frictional sliding on faults containing gouge, *Journal of Structural Geology*, *11*(7), 815–825, doi:10.1016/0191-8141(89)90100-4, 1989.

Nakajima, J., T. Matsuzawa, A. Hasegawa, and D. Zhao, Three-dimensional structure of Vp, Vs, and Vp/Vs beneath northeastern Japan: Implications for arc magmatism and fluids, *J. Geophys. Res.*, *106*(B10), 21,843–21,857, doi:10.1029/2000JB000008, 2001.

Nanjundiah, P., S. Barbot, and S. Wei, Static source properties of slow and fast earthquakes, *Journal of Geophysical Research: Solid Earth*, *125*(12), e2019JB019,028, doi:10.1029/2019JB019028, 2020.

Niemeijer, A., C. Spiers, and C. Peach, Frictional behaviour of simulated quartz fault gouges under hydrothermal conditions: Results from ultra-high strain rotary shear experiments, *Tectonophysics*, *460*(1-4), 288–303, doi:10.1016/j.tecto.2008.09.003, 2008.

Noda, H., and T. Shimamoto, Transient behavior and stability analyses of halite shear zones with an empirical rate-and-state friction to flow law, *Journal of Structural Geology*, *38*, 234–242, doi:10.1016/j.jsg.2011.08.012, 2012.

Okamoto, A. S., A. R. Niemeijer, T. Takeshita, B. A. Verberne, and C. J. Spiers, Frictional properties of actinolite-chlorite gouge at hydrothermal conditions, *Tectonophysics*, *779*, 228,377, doi:10.1016/j.tecto.2020.228377, 2020.

Okazaki, K., and G. Hirth, Deformation of mafic schists from subducted oceanic crust at high pressure and temperature conditions, *Tectonophysics*, *774*, 228,217, doi:10.1016/j.tecto.2019.228217, 2020.

Oleskevich, D., R. Hyndman, and K. Wang, The updip and downdip limits to great subduction earthquakes: Thermal and structural models of cascadia, south alaska, sw japan, and chile, *J. Geophys. Res.*, *104*(B7), 14,965–14,991, 1999.

Peacock, S. M., Thermal and metamorphic environment of subduction zone episodic tremor and slip, *J. Geophys. Res.*, *114*(B8), doi:10.1029/2008jb005978, 2009.

Pec, M., H. Stünitz, R. Heilbronner, and M. Drury, Semi-brittle flow of granitoid fault rocks in experiments, *J. Geophys. Res.*, *121*(3), 1677–1705, doi:10.1002/2015JB012513, 2016.

Peyrat, S., R. Madariaga, E. Buforn, J. Campos, G. Asch, and J. Vilotte, Kinematic rupture process of the 2007 tocopilla earthquake and its main aftershocks from teleseismic and strong-motion data, *Geophys. J. Int.*, *182*(3), 1411–1430, doi:10.1111/j.1365-246X.2010.04685.x, 2010.

Platt, J. P., and W. L. Schmidt, Is the Inverted Field Gradient in the Catalina Schist Terrane Primary or Constructional?, *Tectonics*, *43*(2), doi:10.1029/2023tc008021, 2024.

Platt, J. P., M. Grove, D. L. Kimbrough, and C. E. Jacobson, Structure, metamorphism, and geodynamic significance of the catalina schist terrane, in *From the Islands to the Mountains: A 2020 View of Geologic Excursions in Southern California*, Geological Society of America, doi:10.1130/2020.0059(05), 2020.

Qiu, Q., and S. Barbot, Tsunami excitation in the outer wedge of global subduction zones, *Earth-Science Reviews*, p. 104054, doi:10.1016/j.earscirev.2022.104054, 2022.

Ruina, A., Slip instability and state variable friction laws, *J. Geophys. Res.*, *88*, 10,359–10,370, doi:10.1029/JB088iB12p10359, 1983.

Saffer, D. M., and H. J. Tobin, Hydrogeology and mechanics of subduction zone forearcs: Fluid flow and pore pressure, *Annual Review of Earth and Planetary Sciences*, *39*(1), 157–186, doi:10.1146/annurev-earth-040610-133408, 2011.

Sathiakumar, S., and S. Barbot, The stop-start control of seismicity by fault bends along the Main Himalayan Thrust, *Communications Earth & Environment*, *2*(1), 1–11, doi:10.1038/s43247-021-00153-3, 2021.

Sathiakumar, S., S. Barbot, and J. Hubbard, The role of fault structural evolution on long-term slip rates and seismic cycles in the Himalayan orogenic wedge, *Earth Planet. Sci. Lett.*, *630*, 118,599, doi:10.1016/j.epsl.2024.118599, 2024.

Sawai, M., A. R. Niemeijer, O. Plümper, T. Hirose, and C. J. Spiers, Nucleation of frictional instability caused by fluid pressurization in subducted blueschist, *Geophys. Res. Lett.*, *43*(6), 2543–2551, doi:10.1002/2015gl067569, 2016.

Scholz, C., Microfracturing and the inelastic deformation of rock in compression, *Journal of Geophysical Research*, *73*(4), 1417–1432, doi:10.1029/JB073i004p01417, 1968.

Scholz, C. H., Earthquakes and friction laws, *Nature*, *391*, 37–42, doi:10.1038/34097, 1998.

Skarbek, R. M., and H. M. Savage, RSFit3000: A MATLAB GUI-based program for determining rate and state frictional parameters from experimental data, *Geosphere*, *15*(5), 1665–1676, doi:10.1130/GES02122.1, 2019.

Song, T.-R. A., and M. Simons, Large trench-parallel gravity variations predict seismogenic behavior in subduction zones, *Science*, *301*(5633), 630–633, doi:10.1126/science.1085557, 2003.

Syracuse, E. M., P. E. v. Keken, and G. A. Abers, The global range of subduction zone thermal models, *Phys. Earth Planet. Inter.*, *183*(1-2), 73–90, doi:10.1016/j.pepi.2010.02.004, 2010.

Wada, I., and K. Wang, Common depth of slab-mantle decoupling: Reconciling diversity and uniformity of subduction zones, *Geochemistry, Geophysics, Geosystems*, *10*(10), doi:10.1029/2009GC002570, 2009.

Wang, K., H. Luo, J. He, and M. Carvajal, Soft barrier to megathrust rupture enabled by serpentinized mantle wedge: The chile subduction zone, *Earth Planet. Sci. Lett.*, *650*, 119,115, doi:10.1016/j.epsl.2024.119115, 2025.

Wu, B., and S. Barbot, Evolution of the real area of contact during laboratory earthquakes, *Proc. Nat. Acad. Sci.*, doi:10.1073/pnas.2410496122, 2025.

Yamanaka, Y., and M. Kikuchi, Asperity map along the subduction zone in northeastern japan inferred from regional seismic data, *J. Geophys. Res.*, *109*(B7), doi:10.1029/2003JB002683, 2004.

Ye, L., et al., The 2021 MW 8.1 Kermadec Earthquake Sequence: Great Earthquake Rupture Along the Mantle/Slab Contact, *J. Geophys. Res.*, *130*(4), doi:10.1029/2024jb030926, 2025.

Zeng, H., S. Wei, and H. Yang, The 2021 Mw 8.1 Kermadec Megathrust Earthquake: An Event Rupturing the Slab-Mantle Interface With Up-Dip High-Frequency Seismic Energy Radiation, *Geophys. Res. Lett.*, *52*(4), e2024GL113,015, doi:10.1029/2024GL113015, 2025.

Zhang, H., S. Barbot, and L. Zhang, Data and code for "large megathrust earthquakes in cold mantle wedge corners under lawsonite blueschist facies", doi:10.5281/zenodo.18529749, 2026.

Acknowledgments

We are grateful for the technical support of Wenming Yao and Changrong He at the Institute of Geology, China Earthquake Administration. This study is funded by the National Natural Science Foundation of China under grant 42274234, the National Key Research and Development Program of China (2022YFC3003704) and the National Science Foundation under award number EAR-1848192. H.Z. acknowledges support from the National Science Foundation grant EAR-2041892 awarded to John E. Vidale.

Author Contributions Statement

S.B., H.Z., and L.Z. conceptualized the study. H.Z. and Z.Y. conducted the deformation experiments. H.Z. and S.B. processed the original laboratory data. J.P. conducted the thin section analysis. L.Z. conducted the SEM analysis. M.L. and L.Z. conducted the data analysis. H.Z. and S.B. produced the original manuscript. All the authors reviewed the manuscript.

Competing Interests Statement

The authors declare they have no competing interests.

Table 1: Constitutive parameters used to describe the mechanical behavior of metagreywacke from room temperature to 500°C under 50 MPa to 320 MPa effective normal stress including a pore-fluid pressure of 30 MPa.

Parameter	Symbol	Value	Unit
Area of contact			
Reference friction coefficient	μ_0	0.5	
Reference microasperity size	d_0	1	µm
Microasperity size sensitivity	α	0.06	
Normal stress sensitivity	β	0.3	
Reference normal stress	σ_0	165	MPa
Flow law			
Reference velocity	V_0	1	µm/s
Reference shear strength	τ_0	170	MPa
Stress power exponent	n_1	60	
	n_2	35	
	n_3	23	
Activation energy	Q_1	10	kJ/mol
	Q_2	50	kJ/mol
	Q_3	90	kJ/mol
Activation temperature	T_1^0	20	°C
	T_2^0	280	°C
	T_3^0	280	°C
Compressibility factor	ζ_1	5	
	ζ_2	0	
	ζ_3	0	
Evolution law			
Reference strain-rate	f_0	1	1/s
Active gouge layer thickness	h	1	mm
Characteristic strain	$1/\lambda$	0.02	
Micro-asperity size exponent	p_1	$4\,\alpha n_1$	
	p_2	$0.95\,\alpha n_2$	
Normal stress power exponent	q_1	10	
	q_2	1	
Activation energy	H_1	40	kJ/mol
	H_2	90	kJ/mol
Activation temperature	T_1	0	°C
	T_2	415	°C

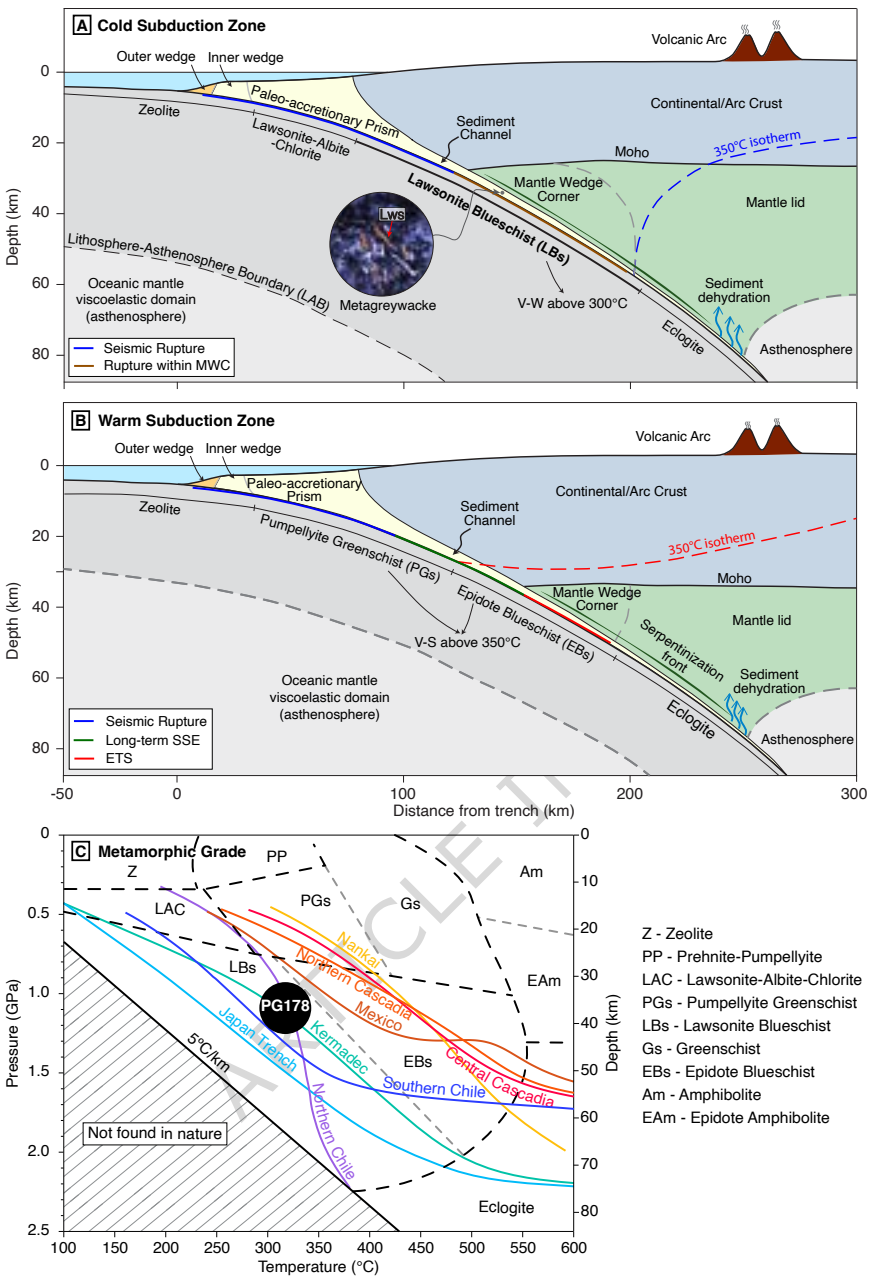

Figure 1: Structural and thermal models of warm and cold subductions zones. a) In cold subduction zones, the mantle wedge corner lies above the 350°C isotherm (blue dashed line). Sedimentary rocks from the accretionary prism can subduct along with the slab through the sediment channel, undergoing metamorphism in the sequence of zeolite, lawsonite-albite-chlorite, lawsonite blueschist, and eclogite facies. Seismic rupture can occur both above the mantle wedge corner (blue thick line) and occasionally within the mantle wedge corner (brown thick line). V-W: velocity weakening. b) In warm subduction zones, the mantle wedge corner is located below the 350°C isotherm (red dashed line). V-S: velocity strengthening. c) Thermal models (color curves) of subduction interfaces and related metamorphic grade [*Syracuse et al.*, 2010; *Gao and Wang*, 2014; *Julve et al.*, 2025]. With a peak temperature of 331 ± 21°C and a peak pressure of 1.06 ± 0.04 GPa, corresponding to $\sim 37 \pm 4$ km, assuming a rock density of 2,800 kg/m^3, the Catalina metagreywacke sample PG178 represents lawsonite-blueschist facies.

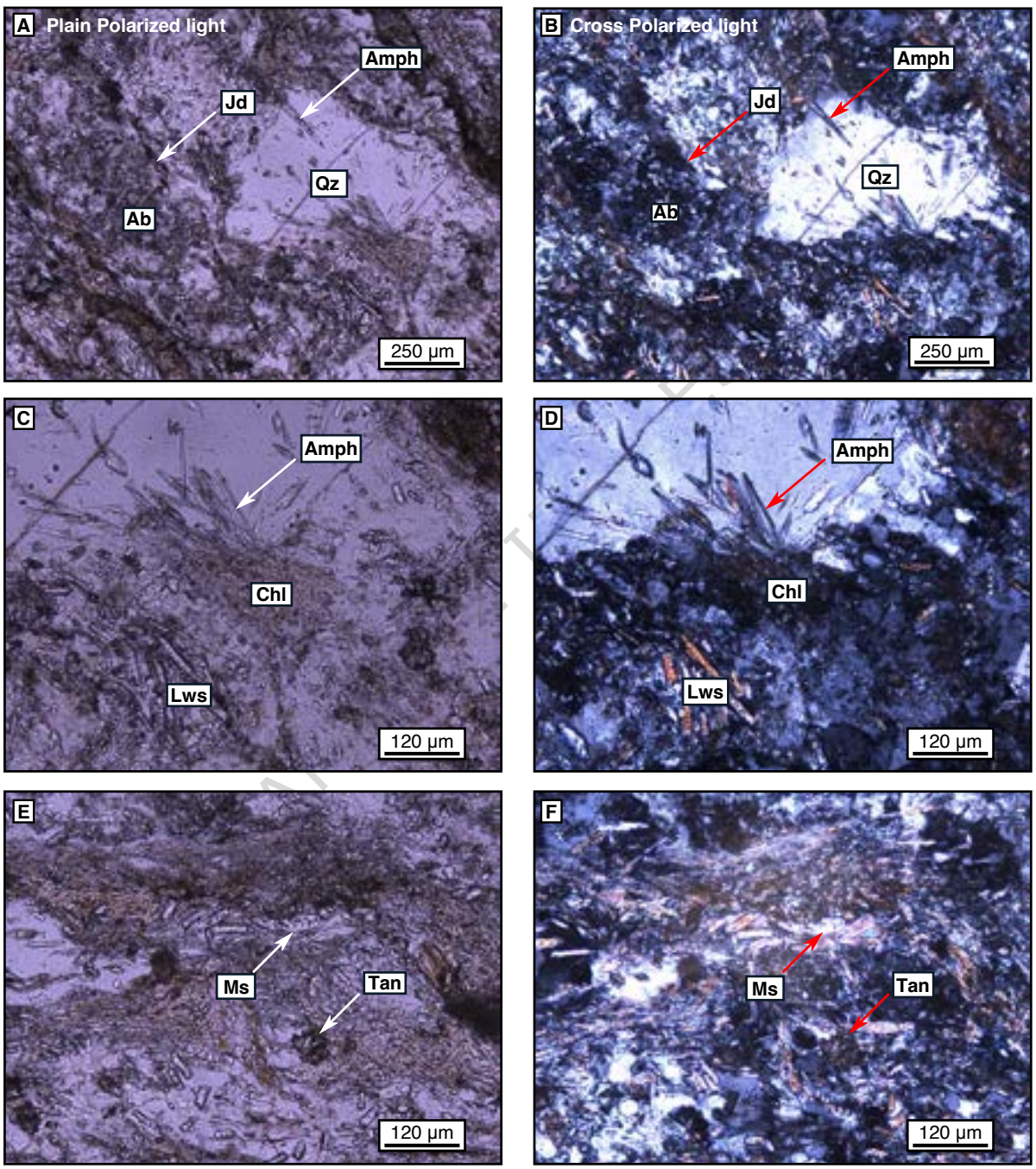

Figure 2: Metagreywacke thin section. a, c, e) Plain Polarized Light (PPL) images and b, d, f) Crossed Polarized Light (XPL) images. The distribution of minerals, especially lawsonite, is indicative of the lawsonite blueschist facies. Ab: albite; Amph: amphibole; Qz: quartz; Lws: lawsonite; Chl: chlorite; Ms: muscovite; Tan: titanite; Jd: jadeite.

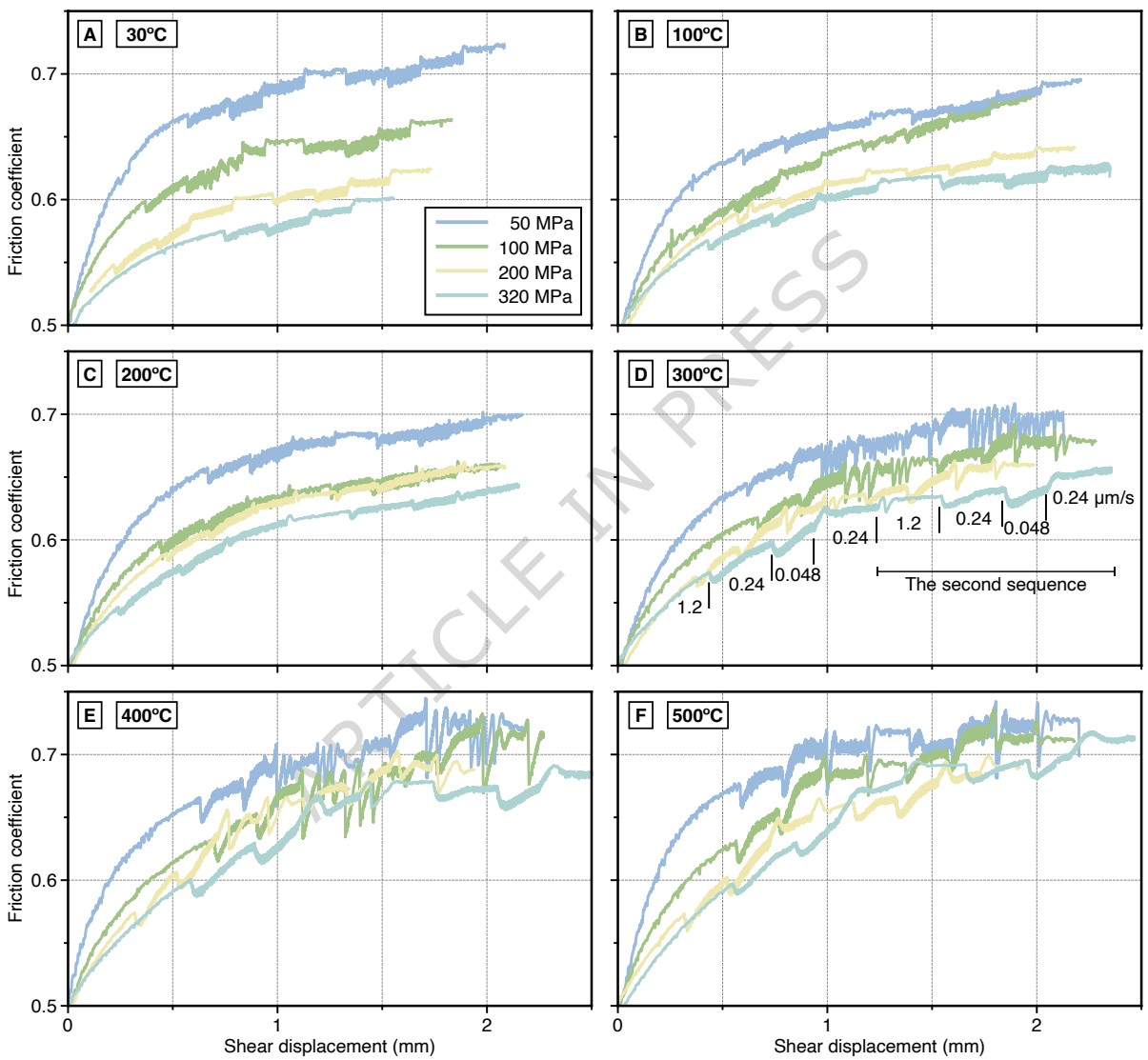

Figure 3: Frictional behavior of metagreywacke during velocity-step experiments under effective normal stress from 50 MPa to 320 MPa and temperatures up to 500°C. a) Experiments at room temperature (30°C). b-f) Experiments at 100-500°C. The colors indicate effective normal stresses. The curves are shifted horizontally for clarity. d) The imposed loading-rate for a representative experiment conducted at 320 MPa is delineated by vertical lines. The other experiments follow the same sequence.

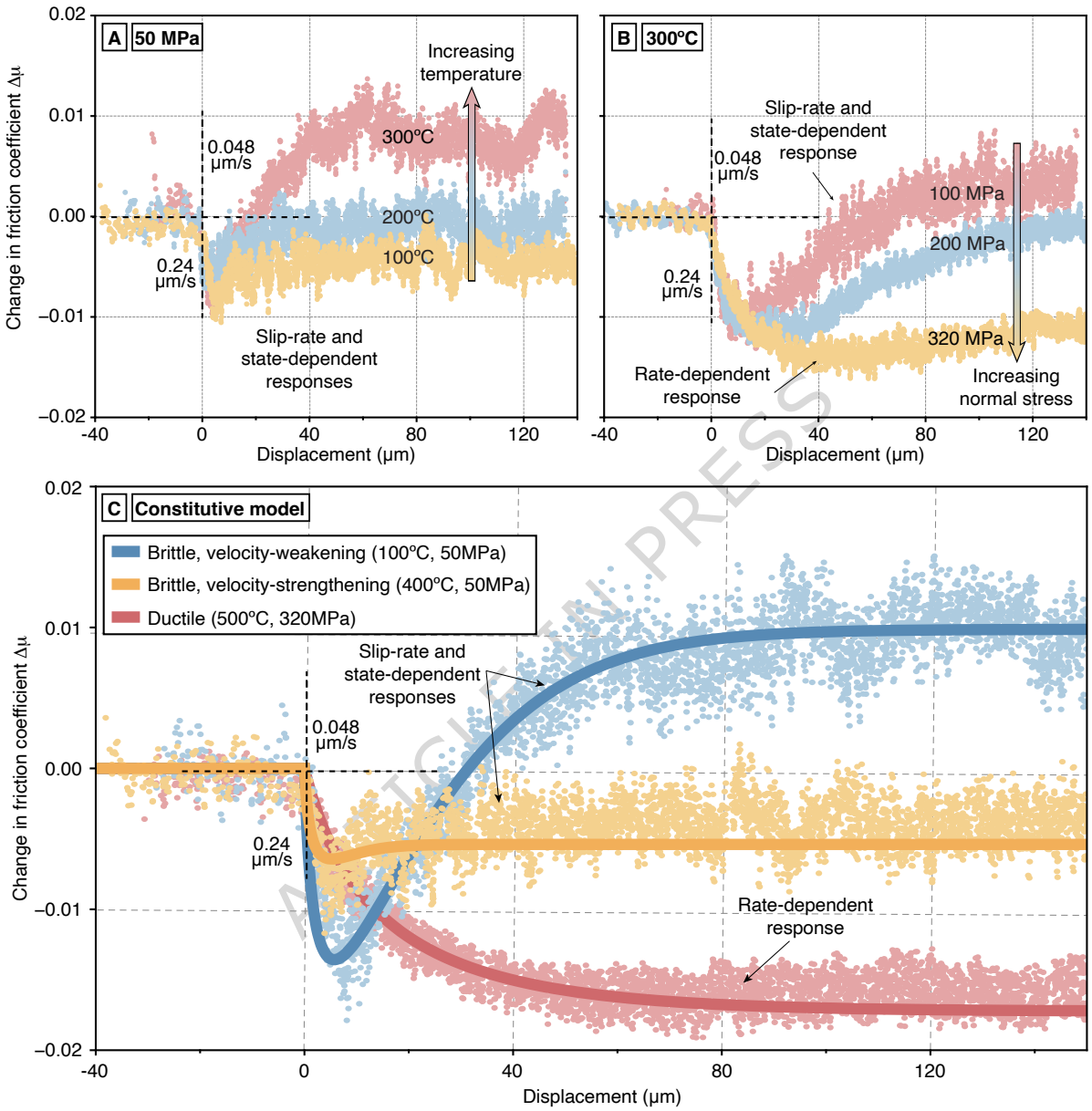

Figure 4: Mechanical regime under various pressure and temperature conditions. a) Transition from velocity-strengthening to velocity-neutral, to velocity-weakening behavior as temperature increases from 100°C to 300°C, under a constant effective normal stress of 50 MPa and a velocity step from 0.24 µm/s to 0.048 µm/s. While the direct effect is similar, the ambient temperature greatly affects the evolutionary phase that follows the velocity step. b) Transition from brittle to ductile behavior as the effective normal stress increases from 100 MPa to 320 MPa under a constant ambient temperature of 300°C for the velocity step from 0.24 µm/s to 0.048 µm/s. Within the ductile behavior, the mechanical response is dominantly rate-dependent, instead of slip-rate- and state-dependent. c) Representative velocity steps across brittle velocity-strengthening (yellow), brittle velocity-weakening (blue), and ductile (red) regimes. The model is based on the constitutive parameters in Table 1 and a machine stiffness of 100 GPa/m.

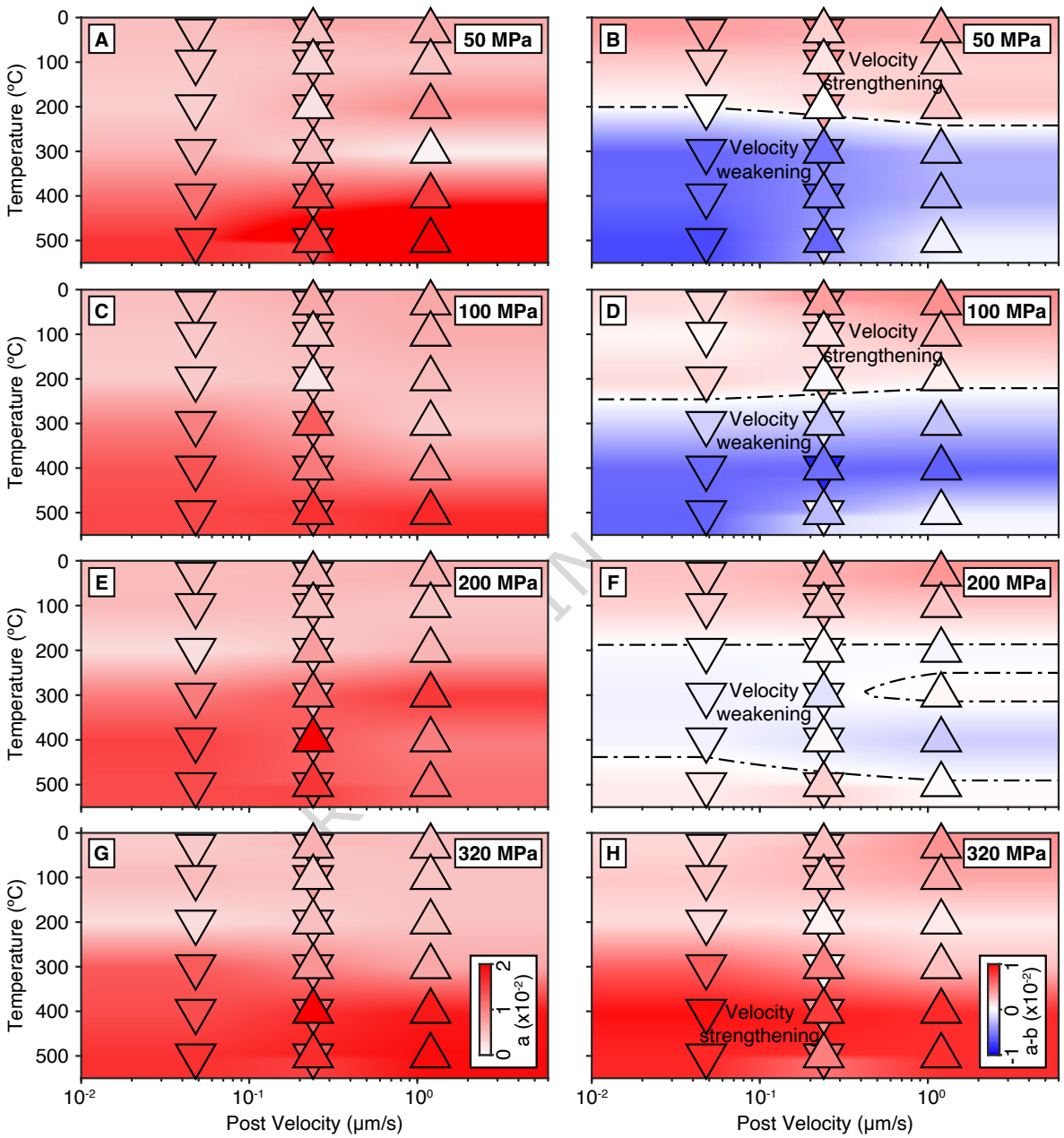

Figure 5: Measured frictional properties of metagreywacke under various temperature, slip-rate, and effective normal stress conditions. a, c, e, and g) Direct effect parameter a for effective normal stress of 50 MPa, 100 MPa, 200 MPa, and 320 MPa, respectively. b, d, f, and h) Estimated steady-state parameter $a - b$ of metagreywacke as a function of post velocity and temperature. The dashed contours correspond to velocity neutral. The laboratory data are shown in upright and downward triangles for up and down velocity steps, respectively. The background color is the interpolation of laboratory data. The post velocity refers to the loading velocity after the velocity step.

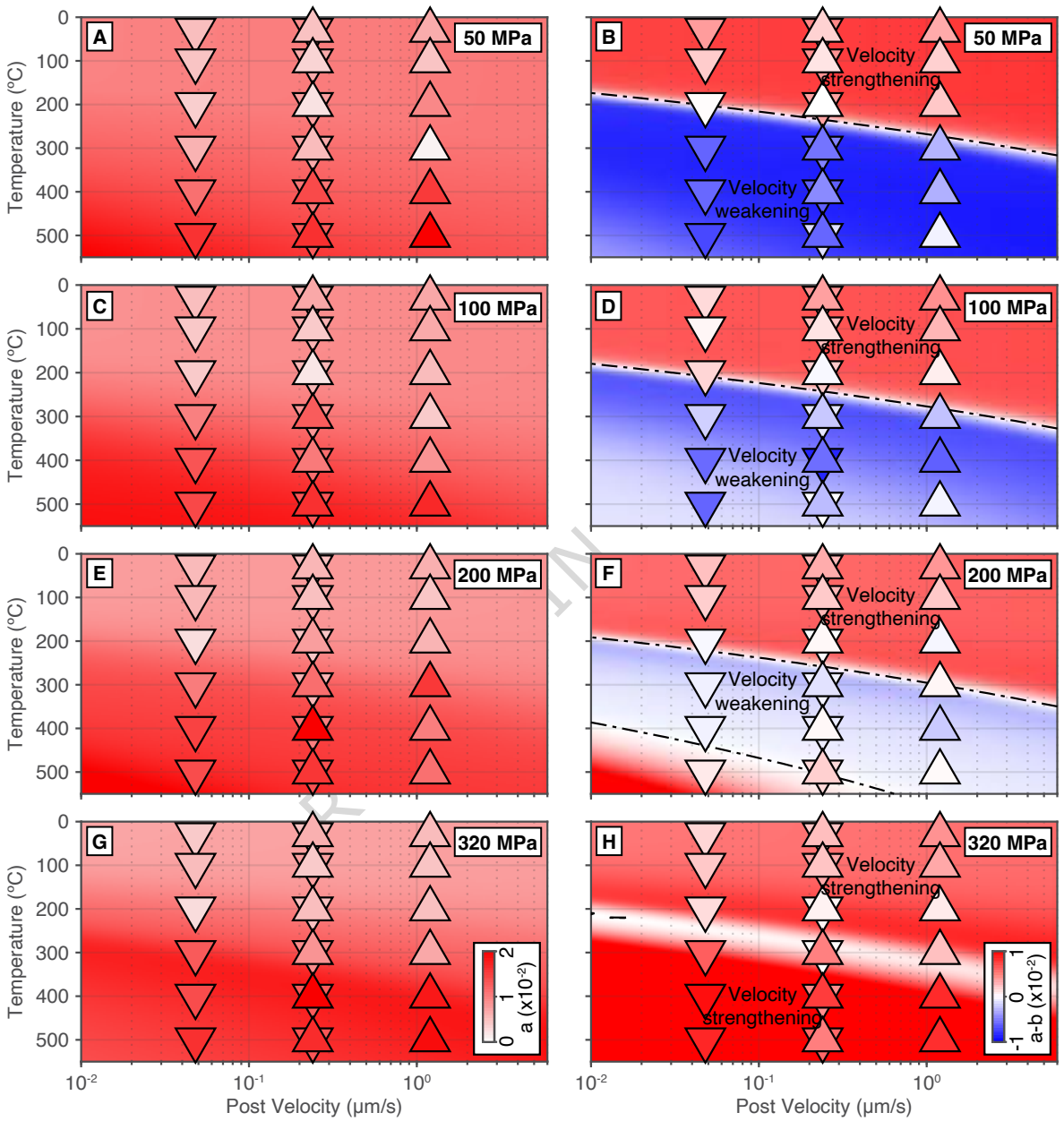

Figure 6: Measured and modeled frictional properties of metagreywacke. a, c, e, g) Measured (triangles) and modeled (background color) direct effect parameter a of metagreywacke as a function of temperature and post velocity for effective normal stress of 50 MPa, 100 MPa, 200 MPa, and 320 MPa, respectively. b, d, f, h) Measured (triangles) and modeled (background color) steady-state parameter $a - b$ of metagreywacke as a function of temperature and post velocity for effective normal stress of 50 MPa, 100 MPa, 200 MPa, and 320 MPa, respectively. The post velocity refers to the second stage of a velocity step.

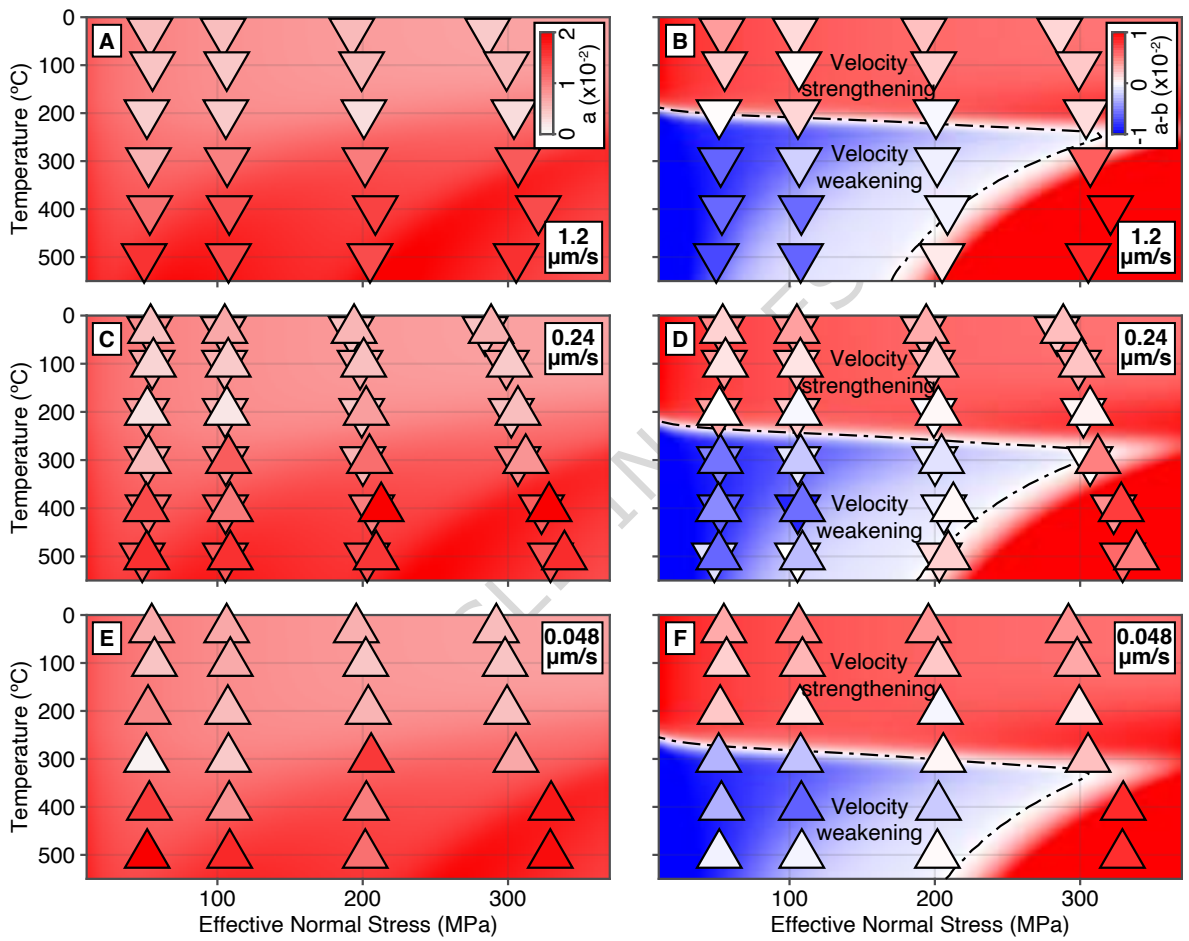

Figure 7: Effect of pressure on the mechanical properties of metagreywacke. a, c, e) Observed (triangles) and modeled (background color) direct effect parameter a as a function of temperature and effective normal stress at post velocities of 1.2 µm/s, 0.24 µm/s, and 0.048 µm/s, respectively. b, d, f) Observed (triangles) and modeled (background color) steady-state parameter $a-b$ of metagreywacke as a function of temperature and effective normal stress at post velocities of 1.2 µm/s, 0.24 µm/s, and 0.048 µm/s, respectively. Post velocity indicates the second stage of the velocity step. Velocity strengthening occurs at low temperature and high pressure conditions.

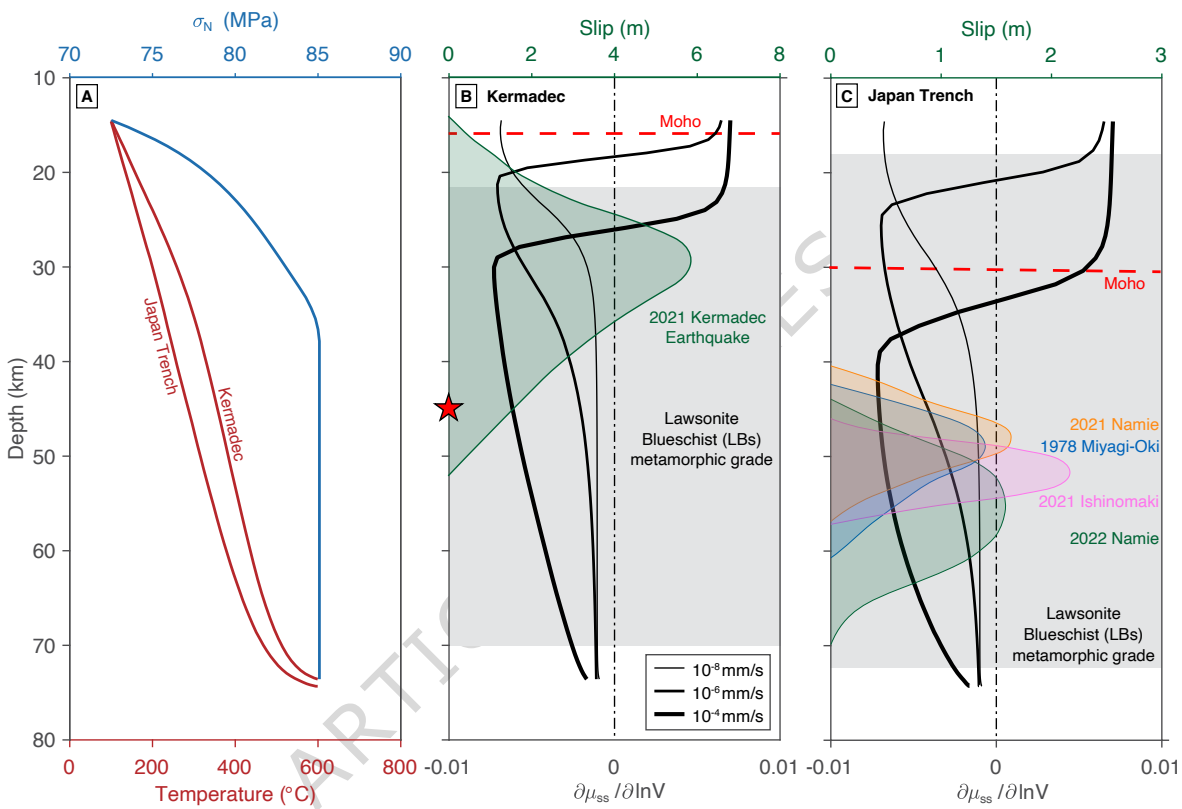

Figure 8: Properties of cold subduction slab interface with depth. a) Thermal structure (red) and effective normal stress (blue) models for the Kermadec and Japan Trench subduction zones. b) Modeling results of $a - b = \partial\mu_{ss}/\partial \ln V$ (black curves) along the Kermadec subduction interface for the slip rates of 10^{-8}, 10^{-6}, and 10^{-4} mm/s. The green line represents the slip distribution of the 2021 M_W 8.1 Kermadec earthquake [*Zeng et al.*, 2025]. The hypocenter of the M_W 7.4 foreshock is marked by a red star. The red dashed line and gray shading indicate the depth of Moho and lawsonite blueschist (LBs) metamorphic grade, respectively. c) Same as b) for the Japan Trench with the slip distribution of the 1978 Miyagi-Oki earthquake [*Yamanaka and Kikuchi*, 2004] and other mantle wedge events [*Goldberg et al.*, 2022].

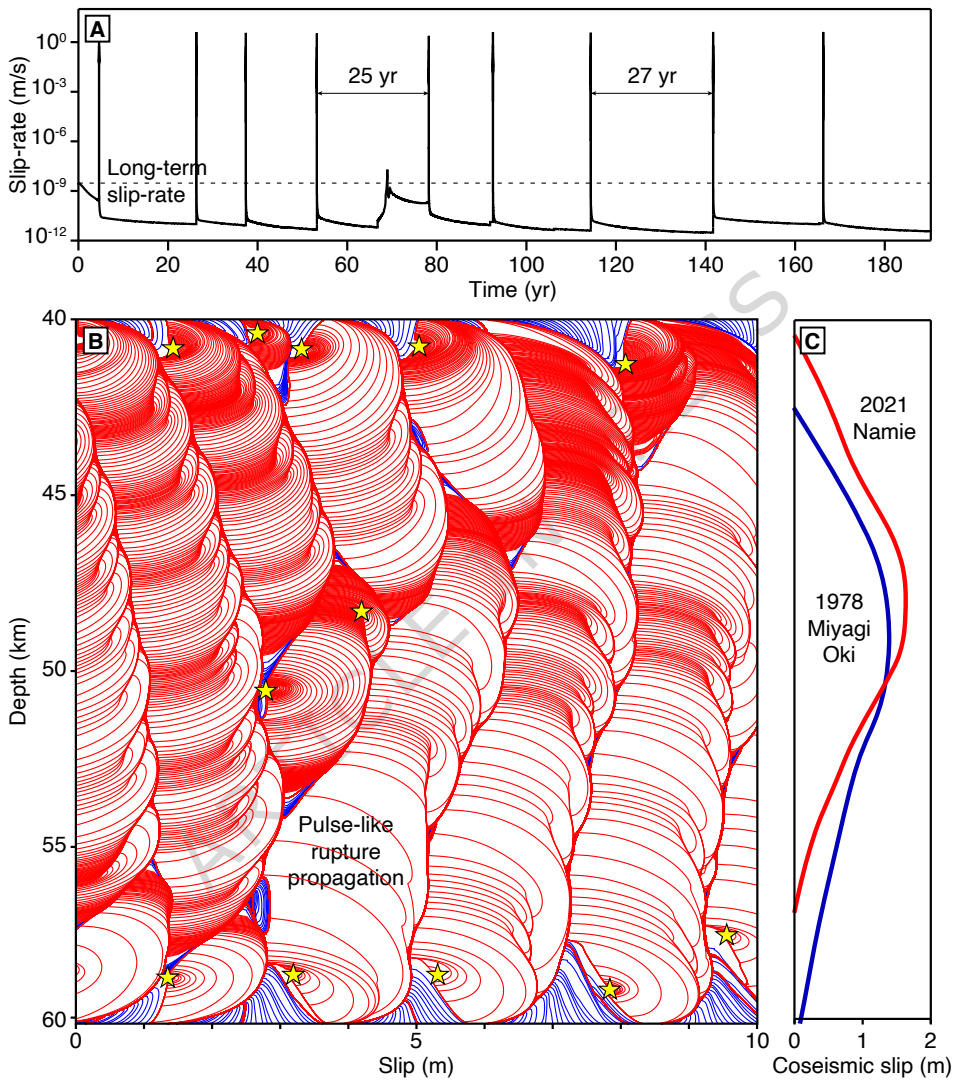

Figure 9: Numerical simulation of seismic cycles for metagreywacke in mantle wedge conditions. a) Time series of fault slip-rate at 50 km depth. The long-term slip-rate is indicated by the horizontal dashed line. b) Evolution of coseismic and interseismic fault slip as a function of depth. The red profiles represent cumulative coseismic slip at 20-s intervals. The blue profiles are cumulative aseismic slip at 1-year intervals taking place during the post- and interseismic periods. Yellow stars mark the hypocenter of earthquakes. c) Depth distribution of the coseismic slip for 1978 Miyagi Oki (blue) and 2021 Namie (red) mantle wedge earthquakes.